

International Journal of Vehicle Performance

ISSN online: 1745-3208 - ISSN print: 1745-3194

<https://www.inderscience.com/ijvp>

Optimisation of commercial bus body frame based on the improved grey wolf and Monte Carlo simulation algorithm

Xiujian Yang, Jinlin Gan

DOI: [10.1504/IJVP.2024.10060872](https://doi.org/10.1504/IJVP.2024.10060872)

Article History:

Received:	05 October 2022
Last revised:	21 February 2023
Accepted:	22 February 2023
Published online:	13 December 2023

Optimisation of commercial bus body frame based on the improved grey wolf and Monte Carlo simulation algorithm

Xiujian Yang* and Jinlin Gan

Faculty of Transportation Engineering,
Kunming University of Science and Technology,
No.727 South Jingming Rd., Chenggong District,
Kunming, 650500, China
Email: yangxiujian2013@163.com
Email: 2437504639@qq.com
*Corresponding author

Abstract: This work aims to study the method of design optimisation of the bus body frame orienting the frontal crashworthiness. The optimal design variables are preliminarily determined based on the frontal crashworthiness analysis. Based on the analysis of correlations between the concerned responses and design variables and the comprehensive contribution analysis, the design variables for optimisation are finally determined. The surrogate model is established by the Latin hypercube design of experiments and the response surface method. The grey wolf (GWO) algorithm is improved by introducing the method of generating initialisation by the Tent mapping and improving the convergence factor by the Sigmoid function. By the improved GWO algorithm, the deterministic optimisation and reliability optimisation are performed and evaluated. The results of finite element analysis reveal that the proposed optimisation scheme can be effectively improved the performance of frontal crashworthiness of the bus body frame with high reliability.

Keywords: design optimisation; bus body frame; crashworthiness; reliability optimisation; TOPSIS; grey wolf algorithm.

Reference to this paper should be made as follows: Yang, X. and Gan, J. (2024) 'Optimisation of commercial bus body frame based on the improved grey wolf and Monte Carlo simulation algorithm', *Int. J. Vehicle Performance*, Vol. 10, No. 1, pp.24–49.

Biographical notes: Xiujian Yang received his BSc and PhD in Mechanical Engineering from Shandong University, China in June 2004 and June 2009, respectively. He is currently working at Faculty of Transportation Engineering, Kunming University of Science and Technology, China. His research interests are vehicle dynamics and control.

Jinlin Gan received his BSc in Transportation Engineering from Kunming University of Science and Technology, China in July 2019. He is currently working toward his Master's in Transportation Engineering in Faculty of Transportation Engineering, Kunming University of Science and Technology, China. His research interests are vehicle CAE and design optimisation.

1 Introduction

With the development of new energy technology, the promotion of environmental protection and low-carbon driving, electric passenger vehicles have gradually become the main transport means for road passengers. The safety of passenger vehicles in collision and the crashworthiness of passenger vehicle structures have received widespread attention in current automotive industry (Sun et al., 2011; Lv et al., 2016; Xia et al., 2018).

The crashworthiness oriented vehicle body design is a complex and nonlinear engineering problem. The crashworthiness safety of vehicle body is affected by a great number of factors. For instance, the variable impact loads generated in the collision would lead to various uncertainties. However, the uncertainty factors may cause the design exceeding the constraint boundaries, and finally lead to unreliable structural design. Therefore, many scholars have conducted reliability research on vehicle body collisions to respond to this problem. By combining the non-dominated sorting genetic algorithm II (NSGA-II) and Monte Carlo Simulation (MCS) methods, reliability-based design optimisation (RBDO) methods were proposed by Lv et al. (2016) and Xia et al. (2018). Gu et al. (2017) calculated the constrained reliability level via the first-order reliability method (FORM) and the second-order reliability method (SORM), respectively. The results of comparison with MCS revealed that the method of SORM is more accurate than FORM. Chen et al. (2013) developed an optimal shifting vector (OSV) method to improve the efficiency of RBDO. Huang et al. (2017) adopted a decoupling strategy in RBDO orienting crashworthiness and thus the optimisation efficiency has been greatly improved.

Generally, it is necessary to consider the design constraint in the optimisation process for body structure design optimisation. To solve such optimisation problems, scholars widely use intelligent optimisation algorithms and find the optimal solution through iteration (Salmani et al., 2022). Among the intelligent optimisation algorithms, particle swarm optimisation (PSO) is one of the most widely used global optimisation methods. However, the main problem with this method is that, it is prone to falling into local optimum and thus not easy to obtain the global optimum solution, resulting in non-uniform distribution of the optimum solution (Kennedy and Eberhart, 1995). It is not easy to obtain the global optimum solution, resulting in uneven distribution of the optimum solution. Non-dominated sorting genetic algorithm (NSGA-II) is another widely used optimisation algorithm with the characteristic of fast convergence speed (Deb et al., 2000). Besides, there are several well-known optimisation algorithms in various fields, including genetic algorithm (GA), ant colony algorithm (ACO), differential evolution (DE), etc. (Mittal et al., 2016). Compared with widely utilised heuristic algorithms such as PSO, DE, and GSA, the grey wolf (GWO) algorithm is much advantageous and has been used in the many fields such as aircraft path planning, cluster analysis, economic scheduling problems, and feature subsets selection etc. (Mirjalili et al., 2014; Zhang and Wang, 2019).

Although the GWO algorithm presents some certain advantages, it also has shortcomings, such as being easy to fall into the local optimum solution, strong dependence on the initial population, and premature convergence (Xu et al., 2017). Focusing on the above problems, many scholars have done much work to improve the GWO algorithm. The most common way to improve is to adjust the algorithm parameters or modify the position updating formula, to improve the algorithm convergence speed

meanwhile avoiding the algorithm from falling into the local optimum. Mittal et al. (2016) tuned the parameters of the GWO algorithm by different functions with various slopes. Long et al. (2018) proposed the ROL-GWO algorithm by modifying the parameter 'C' in the GWO algorithm. In addition, the author also modified the position update mechanism of the GWO algorithm and proposed the EEGOW algorithm (Long et al., 2019). Some scholars try to add some search strategies to the algorithm to improve its performance. For instance, in Wei et al. (2017), the optimal guided search equation is introduced into the GWO algorithm, making the algorithm more adaptive. Moreover, the algorithm performance can also be improved by combining the algorithms according to the advantages and disadvantages of each algorithm. For example, Gaidhane and Nigam (2018) propose a GWO-ABC algorithm by leveraging the advantages of GWO and artificial bee colony (ABC). Similarly, there are other combinations, such as PSO and GWO (Kamboj, 2016), DE and GWO, etc. (Zhu et al., 2015).

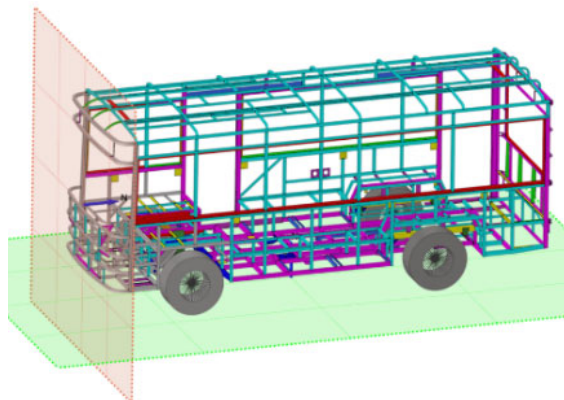
The studies mentioned above show that most of the optimising design algorithm has its own limitations and advantages. Indeed, the improved algorithm can improve the performance of some problems, but it does not mean that all the optimisation problems can be solved perfectly. In this work, an optimising design method for the safety of frontal crashworthiness of the electric bus body frame is proposed based on the improved GWO algorithm.

2 Crashworthiness finite element model and design variables

2.1 *Crashworthiness finite element model*

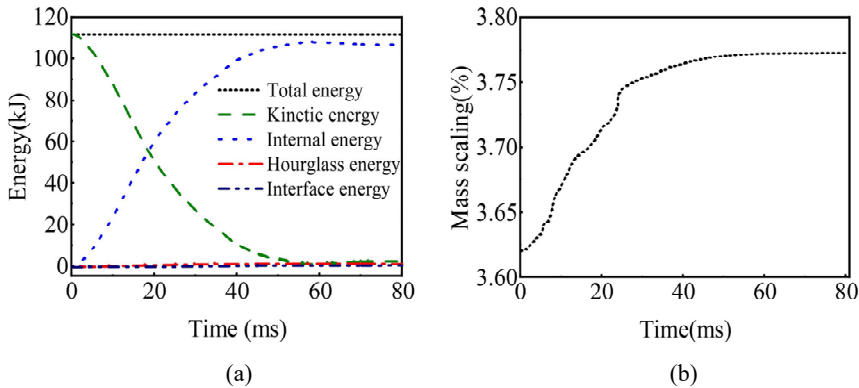
Based on the Hypermesh/LS-DYNA software, the finite element model for an electric bus body frame is established, ignoring the related electrical equipment, glass and decorations, and the body skin. The simplified crashworthiness finite element model of the commercial electric bus body frame is shown in Figure 1. The model contains 587629 mesh elements and 582572 nodes, and the total mass is 1142.47kg.

Figure 1 Frontal crashworthiness model of the electric bus body frame (see online version for colours)



In this paper, following the requirements of the frontal collision test of automobiles in ‘Occupant Protection in Frontal Collision of Automobiles’ (National Standard of China GB11551-2014), the finite element simulation of a 100%-frontal-rigid collision at a speed of 50km/h is carried out, and the simulation time is 80ms. In the finite element analysis, due to the characteristics of the element or the material parameter settings, the time step of the element may be smaller than the minimum time step set in the card resulting in the scaling of mass. Figure 2 shows the collision energy curve and mass scaling curve. According to the requirements of the law of energy conservation, the total energy remains unchanged in an effective collision. The total energy is composed of kinetic energy, internal energy, hourglass energy and slip interface energy, in which the slip interface energy is produced by friction and damping. Sharp slippage would produce large positive slip interface energy, but undetected penetrations which are not detected in the model would produce large negative slip interface energy. Additionally, Hourglass energy is the energy cost in resisting the deformation caused by the Gaussian single-point integration method adopted in the software calculation. It can be found that the kinetic energy decreases and meanwhile the internal energy increases, and eventually the internal energy tends to be constant when the kinetic energy decreases to zero. Moreover, the sliding interface energy meets the requirement that it should be less than 5% of the total energy. It can be observed that at the moment of 80ms, the total collision energy is 111,687J, and the collision sliding interface energy is 737.374J, accounting for 0.66% of the total energy; meanwhile, the mass increases with a maximum scaling of 3.77%. Since the proportions are all within 5% of the legal requirements, it is reasonably to believe that the established crashworthiness finite element model is effective and can be used for subsequent research.

Figure 2 Variation of energy and mass in collision, (a) energy variation curve (b) mass scaling curve (see online version for colours)



2.2 Preliminary selection of the optimisation variables

During the 100% frontal collision, the electric bus body frame can be divided into energy absorption area, solid area and rear end energy absorption area according to the deformation. The front-end energy absorption area offers the major energy absorption function, and most of the remaining energy unabsorbed is transmitted to the rear through the lower structure of the body frame. By evaluating the energy absorption of the front-

end energy absorption area, the components in the energy-absorbing area and the solid area are mainly chosen for optimisation to ensure that the driver has enough living space. To comprehensively consider the deformation and energy absorption of each energy-absorbing component, ten groups of component are preliminarily selected for optimisation and the corresponding ten thickness parameters are selected as the variables of design optimisation (see Figure 3 and Table 1 for details).

Figure 3 Illustration of the components preliminarily selected for optimisation (see online version for colours)

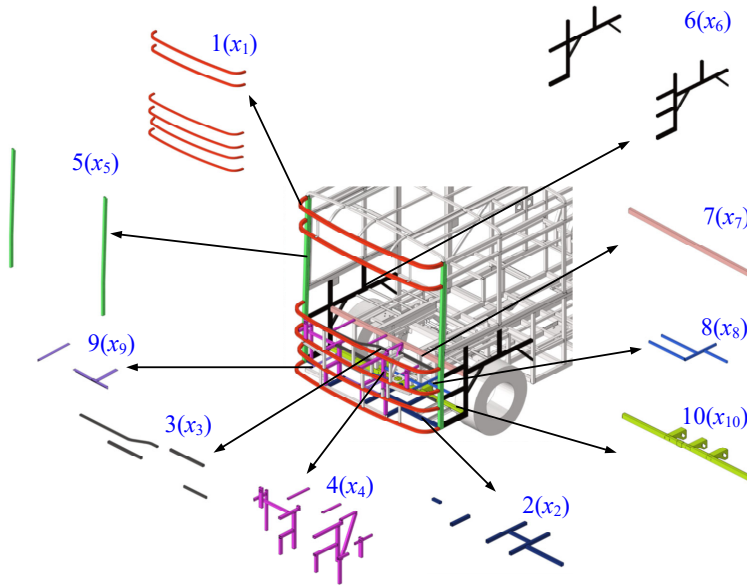


Table 1 Parameters of the components preliminarily selected for optimisation

	<i>Component name</i>	<i>Sectional dimension (mm)</i>	<i>Thickness (mm)</i>
x_1	Front sash beam and front girldle beam	38.5×38.5	1.5
x_2	Cockpit bottom frame	38.5×38.5	1.5
x_3	Instrument panel beam	18.5×28.5	1.5
x_4	Front girth post and beam	38.5×38.5	1.5
x_5	Front window post	28.5×38.5	1.5
x_6	Cockpit side frame	38.5×38.5	1.5
x_7	Frame beam	38×58	2
x_8	Middle cockpit frame	19×29	1
x_9	Bottom transverse stringer	28×38	4
x_{10}	Frame cantilever beam	38×58	4

The maximum total absorbed internal energy of the preliminarily selected optimised component reaches 86686.5J, accounting for 80.2% of the total internal energy as shown in Figure 4. Thus, it is believed that the frontal crashworthiness performance is expected to be considerably improved by optimising the selected components. Referring to

‘Protection of Occupants in the Cab of Commercial Vehicles’ (National Standard of China GB26512-2021), the design of the cab should eliminate the danger to the cab occupants as much as possible in a frontal collision. In this paper, as shown in Figure 5, three measurement points are selected to measure the intrusions, including the steering wheel centre position for measuring the intrusion I_1 , the front of the cockpit for measuring the intrusion I_2 , and the rear of the cockpit for measuring the intrusion I_3 . The intrusion amount refers to the displacement of each measuring point along the collision direction. Besides, the total internal energy absorption energy E of the front-end energy absorption area and the total mass M of the selected ten groups of components for optimisation are utilised as the response.

Figure 4 Maximum energy absorption and proportion of each selected group of component (see online version for colours)

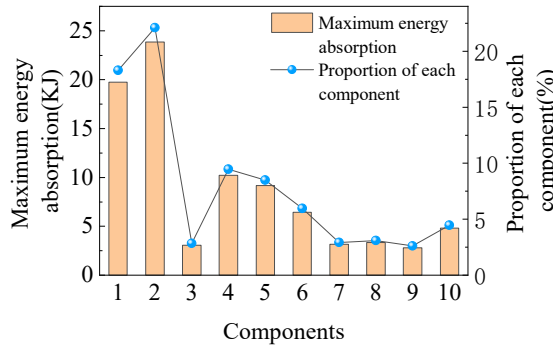
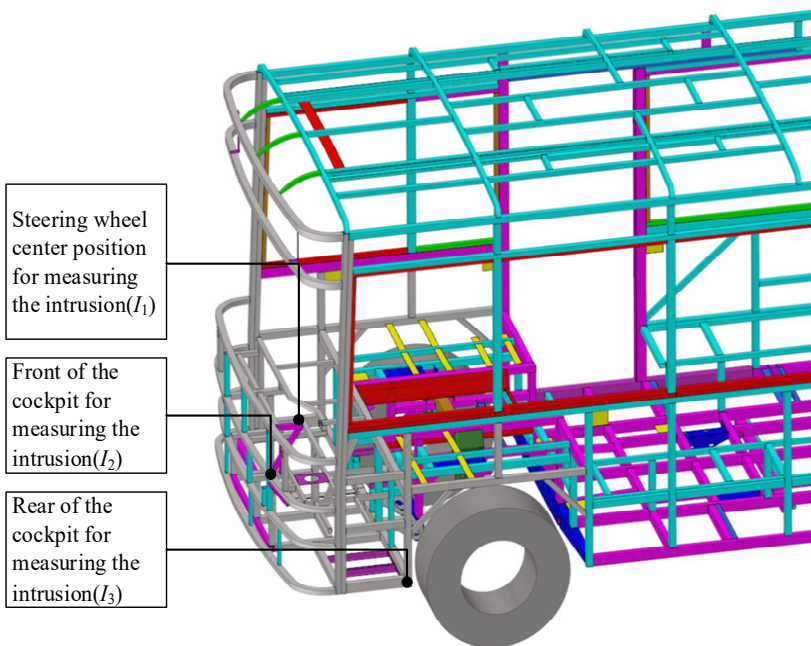


Figure 5 Three measurement points for measuring the intrusions (see online version for colours)



2.3 Determination of the variables for design optimisation

Firstly, 60 sets of experiment are designed for the ten thickness variables x_1, x_2, \dots, x_{10} by using the Latin hyper-dimension method. The upper and lower limits of each thickness variable are set to be 50% of the initial value for the rationality of subsequent fitting. The GRA analysis method is adopted to verify the correlation between the design variables and the optimisation response and to improve the optimisation efficiency in this study. The relative strength of an item affected by other item factors can be judged by the GRA method, based on the similarity and difference of the varying trend of the elements (Li et al., 2019).

The grey correlations between the 10 thickness variables and the 5 output responses obtained through the GRA calculation are illustrated in Table 2. It is believed that the closer the grey correlation coefficient is to 1, the higher the correlation will be. It is seen from Table 1 that the correlations all exceed 0.5, and most of them remain above 0.6. Thus, the thickness variables corresponding to the selected components can better reflect the changes in optimisation response.

Table 2 Grey correlation between design variables and optimisation response

Design variables	Optimisation response				
	I_1	I_2	I_3	E	M
x_1	0.5868	0.5990	0.6744	0.5983	0.5931
x_2	0.5952	0.6047	0.6844	0.5833	0.5884
x_3	0.5963	0.6036	0.6521	0.5773	0.5725
x_4	0.6015	0.6002	0.6815	0.5883	0.5872
x_5	0.5990	0.6127	0.7007	0.5876	0.5833
x_6	0.5880	0.5997	0.6623	0.5945	0.5786
x_7	0.5979	0.5992	0.6402	0.5927	0.5994
x_8	0.6043	0.6020	0.6879	0.5897	0.6048
x_9	0.6148	0.6211	0.6419	0.5812	0.5947
x_{10}	0.5673	0.5676	0.6275	0.6152	0.6158

The entropy weight method and the TOPSIS method are adopted to further evaluate the degree of correlation between the design variables and the optimisation response, and determine the influence of each design variable on the response. The specific calculations are described as follows.

- 1 Calculate the data normalisation as

$$r_{ij} = \frac{x_{ij}}{\sqrt{\sum_{i=1}^m x_{ij}^2}}, \quad (1)$$

where x_{ij} is the grey correlation degree of the i^{th} ($i = 1, 2, \dots, m$) design variable to the j^{th} ($j = 1, 2, \dots, n$) performance index; m is the number of design variables, and n is the number of optimised responses.

- 2 The proportion p_{ij} corresponding to the i^{th} design variable in the j^{th} optimisation response is calculated as

$$p_{ij} = \frac{r_{ij}}{\sum_{i=1}^m r_{ij}}, \quad (2)$$

- 3 Calculate the entropy value e_j of the j^{th} optimisation response as

$$e_j = -\frac{1}{\ln(m)} \sum_{i=1}^m p_{ij} \ln(p_{ij}), \quad (3)$$

- 4 Calculate the weight coefficient w_j for each optimisation response as

$$w_j = \frac{1 - e_j}{\sum_{j=1}^n (1 - e_j)}, \quad (4)$$

- 5 By constructing the decision matrix, the positive and negative ideal solutions Z^+ , Z^- can be calculated as follows:

$$v_{ij} = w_j r_{ij}, \quad (5)$$

$$Z^+ = \begin{cases} \max_{1 \leq i \leq m} v_{ij} & j = 1, 2, \dots, n \\ \min_{1 \leq i \leq m} v_{ij} & j = 1, 2, \dots, n \end{cases}, \quad (6)$$

$$Z^- = \begin{cases} \max_{1 \leq i \leq m} v_{ij} & j = 1, 2, \dots, n \\ \min_{1 \leq i \leq m} v_{ij} & j = 1, 2, \dots, n \end{cases}, \quad (7)$$

Additionally, the Euclidean distance D_i^+ , D_i^- between each design variable and the positive and negative ideal solutions is respectively expressed as

$$D_i^+ = \sqrt{\sum_{j=1}^m (Z_j^+ - v_{ij})^2}, \quad (8)$$

$$D_i^- = \sqrt{\sum_{j=1}^m (Z_j^- - v_{ij})^2}, \quad (9)$$

- 6 Calculate the proximity η of each design variable to the optimisation response as

$$\eta = \frac{D_i^-}{D_i^+ + D_i^-}, \quad (10)$$

Note that the proximity η could be regarded as the contribution coefficient of each design variable to the optimisation response. The larger the proximity η is, the closer the correlation between the design variable and the optimisation response would be.

The calculation results are shown in Table 3, wherein D_i^+ and D_i^- represent the Euclidean distance between each design variable and the positive and negative ideal solutions, and η represents the closeness. The degree of closeness η can be considered as the contribution coefficient of each design variable to the response. The larger η is, the greater the correlation between the design variable and the response will be.

In addition, except design variable x_8 the closeness of which exceeds 0.3, the closeness of the top five design variables to the response is relatively balanced. Combined with Table 1, it can be seen that there is a clear correlation between the top five design variables and the optimal response. Therefore, the top five design variables are chosen for subsequent optimisation to reduce the workload of optimisation. The top five design variables include x_8, x_7, x_4, x_5 and x_3 .

Table 3 Comprehensive contribution analysis

<i>Design variables</i>	<i>D+</i>	<i>D-</i>	<i>η</i>	<i>Sequence</i>
x_1	0.050	0.012	0.068	7
x_2	0.050	0.014	0.074	6
x_3	0.044	0.014	0.082	5
x_4	0.040	0.019	0.109	3
x_5	0.051	0.017	0.084	4
x_6	0.055	0.009	0.048	9
x_7	0.037	0.020	0.120	2
x_8	0.005	0.056	0.313	1
x_9	0.053	0.011	0.059	8
x_{10}	0.054	0.008	0.043	10

3 Formulation of surrogate model

Focusing on the frontal crashworthiness, the response surface methodology (RSM) method is adopted here to fit the surrogate model for the electric bus body frame. RSM as a statistical method uses multivariable quadratic regression equations to fit and solve the multivariate problems. It can also connect the input variables with the response characteristics through a high-order model, and thus is more suitable for nonlinear problems (Gurumoorthy et al., 2020). The common second-order polynomial response surface function expression is described as follows:

$$Y = a_0 + \sum_{i=1}^n a_i X_j + \sum_{i=1}^{n-1} \sum_{j=i+1}^n a_{ij} X_i X_j + \sum_{i=1}^n a_{ii} X_i^2 + \zeta, \tag{11}$$

where X_1, X_2, \dots, X_j are design variables; a_0, a_i, a_{ii}, a_{ij} are undetermined coefficients; n represents the number of design variables; ζ denotes the observation error and noise; Y is the response surface fitting function. This study establishes five response surface models, including three intrusions $I_1(x), I_2(x)$ and $I_3(x)$, energy absorption $E(x)$ of the front-end energy absorption area, and total mass $M(x)$ of the five groups of optimising components.

The method of mutual cross detection is adopted to evaluate the accuracy of the surrogate model. The scatter plot for the predicted and the simulation value is shown in Figure 6. The closer the scatter point is to the 45° line, the higher the fitting accuracy will be. Besides the scatter plot, the fitting degree R^2 is also utilised to evaluate the fitting accuracy of the model, the calculation formula of which is given as follows:

$$R^2 = 1 - \frac{\sum_{p=1}^{n_{\text{test}}} (y_p - \bar{y}_p)^2}{\sum_{p=1}^{n_{\text{test}}} (y_p - \bar{y})^2}, \quad (12)$$

where n_{test} is the number of random samples used to test the accuracy of the approximate model; y_p and \bar{y}_p represents the actual response value and predicted response value of the p^{th} sample point, respectively; \bar{y} is the mean of the actual response values. The calculation results of the fitting degree R^2 are shown in Table 4. It can be seen that the values of R^2 of the five optimised responses all exceed 90%, that is the fitting accuracy is relatively high. Thus, the surrogate model can be used instead of the finite element model for design optimisation.

Figure 6 Scatter plot of the response surface model (see online version for colours)

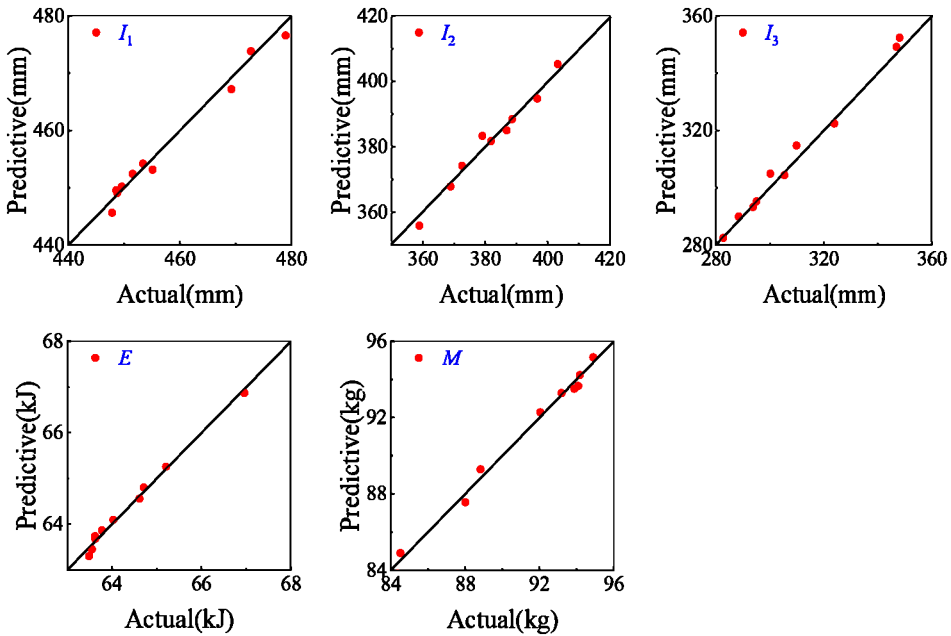


Table 4 Fitting accuracy (R^2) of the response surface model

	I_1	I_2	I_3	E	M
R^2	0.90	0.93	0.91	0.92	0.92

4 Optimisation algorithm

4.1 GWO algorithm

The GWO algorithm is a new swarm intelligence algorithm of optimisation inspired by the predation behaviour of grey wolves. The hunting process of wolves comprises encircling and attacking and can be mathematically described as follows (Mirjalili et al., 2014):

- 1 Wolves surround their prey

$$\mathbf{D} = |\mathbf{C} \cdot \mathbf{X}_p(t) - \mathbf{X}(t)|, \quad (13)$$

$$\mathbf{X}(t+1) = \mathbf{X}_p(t) - \mathbf{A} \cdot \mathbf{D}, \quad (14)$$

wherein equation (13) represents the distance between the grey wolf and its prey, and equation (14) is the position update formula; $\mathbf{X}_p(t)$ represents the position of the prey in the t^{th} generation; $\mathbf{X}(t)$ represents the individual grey wolf in the t^{th} generation. The coefficient vectors \mathbf{A} and \mathbf{C} can be calculated as

$$\mathbf{A} = \mathbf{a}(2\mathbf{r}_1 - 1), \quad (15)$$

$$\mathbf{C} = 2\mathbf{r}_1, \quad (16)$$

where \mathbf{a} is the convergence factor, which decreases linearly from 2 to 0 with the iteration; \mathbf{r}_1 is a random number in the interval $[0, 1]$.

- 2 Once the prey is found, the wolves would attack it. At this time, the α wolf, β wolf, and δ wolf are the closest to the prey, and other wolves will move closer to them. The distance of α wolf, β wolf and δ wolf to other individuals is respectively calculated as

$$\begin{cases} \mathbf{D}_\alpha = |\mathbf{C}_1 \cdot \mathbf{X}_\alpha - \mathbf{X}| \\ \mathbf{D}_\beta = |\mathbf{C}_2 \cdot \mathbf{X}_\beta - \mathbf{X}|, \\ \mathbf{D}_\delta = |\mathbf{C}_3 \cdot \mathbf{X}_\delta - \mathbf{X}| \end{cases} \quad (17)$$

where $\mathbf{X}_\alpha, \mathbf{X}_\beta, \mathbf{X}_\delta$ represents the current position of α wolf, β wolf and δ wolf, respectively; $\mathbf{C}_1, \mathbf{C}_2, \mathbf{C}_3$ are random vectors, \mathbf{X} is the position of the current Grey Wolf. The step size and direction of the individual ω wolf towards the α wolf, β wolf and δ wolf is calculated as follows

$$\begin{cases} \mathbf{X}_1 = \mathbf{X}_\alpha - \mathbf{A}_1 \cdot \mathbf{D}_\alpha \\ \mathbf{X}_2 = \mathbf{X}_\beta - \mathbf{A}_2 \cdot \mathbf{D}_\beta, \\ \mathbf{X}_3 = \mathbf{X}_\delta - \mathbf{A}_3 \cdot \mathbf{D}_\delta \end{cases} \quad (18)$$

The final position of the ω wolf can be thereby derived by

$$\mathbf{X}(t+1) = \frac{\mathbf{X}_1 + \mathbf{X}_2 + \mathbf{X}_3}{3}. \quad (19)$$

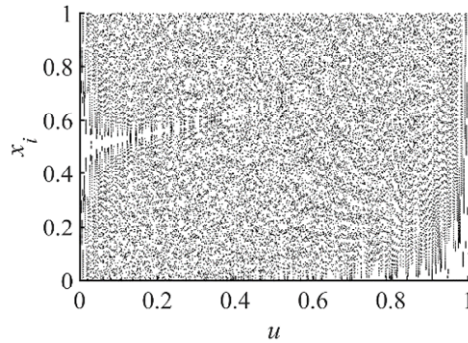
4.2 Improved GWO algorithm

Randomly generating the initialised population may cause uneven population distribution and cannot ensure group diversity, and thereby affects the result of optimisation. However, owing to the randomness characteristics of the chaotic motion, the algorithm can jump out of the local optimum solution during the optimisation, and thus improve the global search ability. Common chaotic mappings include tent mapping, logistic mapping, *etc.* Since logistic mapping is relatively simple, it is widely adopted in the research. It is proved that the uniformity of tent mapping is better than that of logistic mapping (Shan et al., 2005). Thus, in this work tent mapping is utilised to initialise the population, and the mathematical expression is given as

$$x_{i+1} = \begin{cases} \frac{x_i}{u}, & 0 \leq x_i < u \\ \frac{1-x_i}{1-u}, & u \leq x_i \leq 1 \end{cases}, \quad (20)$$

where the relationship between u and the chaotic value x is shown in Figure 7. It can be seen that when $u \geq 0.5$, the mapping has good chaotic properties and the value is relatively uniform (Teng et al., 2018). In this paper, we assume $u = 0.7$.

Figure 7 Impact of u on the chaotic property



It can be seen from equation (14) and equation (15) that the convergence factor a is closely related to the search ability of the algorithm. However, the characteristic that the number of iterations linearly decreases cannot reflect the search ability of the algorithm. To balance the local and global search ability of the algorithm, the linear factor needs to be improved (Al-Omari et al., 2005; Qin and Jiang, 2006). The Sigmoid function is employed to improve the linear convergence factor, and its characteristics are displayed in Figure 8. By the sigmoid function, the convergence speed of the algorithm at the beginning and the end of the convergence becomes slow, and thereby the realisation of avoiding premature convergence and missing the global optimum solution can be done. The specific flow chart of the improved GWO algorithm is illustrated in Figure 9.

Figure 8 Comparison of three convergence factors (see online version for colours)

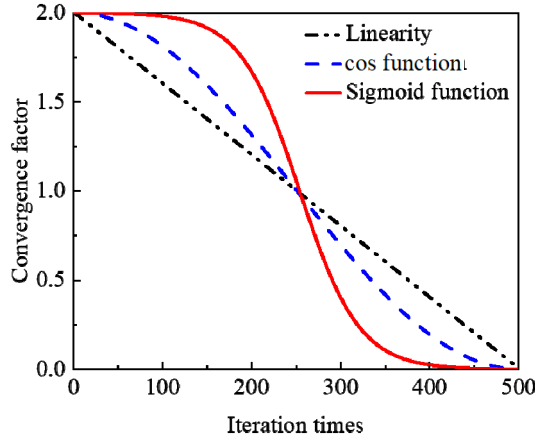
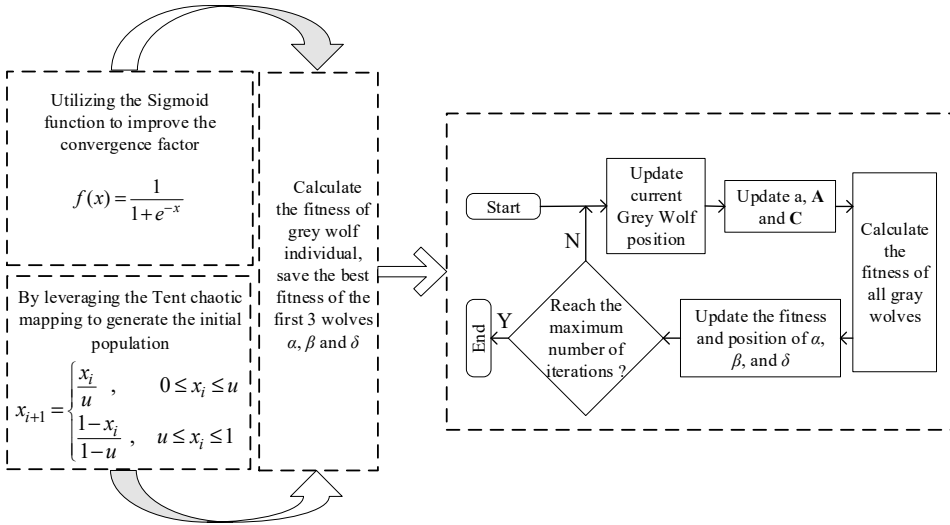


Figure 9 Flow chart of the improved GWO algorithm



4.3 Simulation and analysis

To evaluate the performance of the improved GWO algorithm, four standard test functions $f_1(x) \sim f_4(x)$ presented in Table 5 are selected for simulation experiments (Mirjalili et al., 2014). $f_1(x) \sim f_4(x)$ refers to the function of Sphere, Schwefel, Ackley, and Griewank, respectively. Wherein Sphere and Schwefel are unimodal functions, and Ackley and Griewank are multimodal functions. The four test functions are all of 30-dimension, and the theoretically optimal solutions all are zeros. The plots of the two-dimensional spatial characteristics of the functions are shown in Figure 10. Simulation experiments are conducted for the algorithms comprising the improved GWO, the standard GWO and the traditional particle swarm (PSO). The population size of the

three algorithms is 50, the maximum number of iterations is 500, and the learning factor is set as $c_1 = c_2 = 2$ in the PSO algorithm. For each algorithm, the corresponding test function program was run 30 times and the mean and standard deviation are recorded. The results are shown in Table 6.

Table 5 Test functions

Expression	Search range
$f_1(x) = \sum_{i=1}^n x_i^2$	[-100, 100]
$f_2(x) = \max_i \{ x_i , 1 \leq i \leq n\}$	[-100, 100]
$f_3(x) = -20 \exp\left(-0.2 \sqrt{\frac{1}{n} \sum_{i=1}^n x_i^2}\right) - \exp\left(\sqrt{\frac{1}{n} \sum_{i=1}^n \cos(2\pi x_i)}\right) + 20 + e$	[-32, 32]
$f_4(x) = \frac{1}{4000} \sum_{i=1}^n x_i^2 - \prod_{i=1}^n \cos\left(\frac{x_i}{\sqrt{i}}\right) + 1$	[-50, 50]

Figure 10 Two-dimensional feature spaces of four standard test functions, (a) sphere (b) Schwefel (c) Ackley (d) Griewank (see online version for colours)

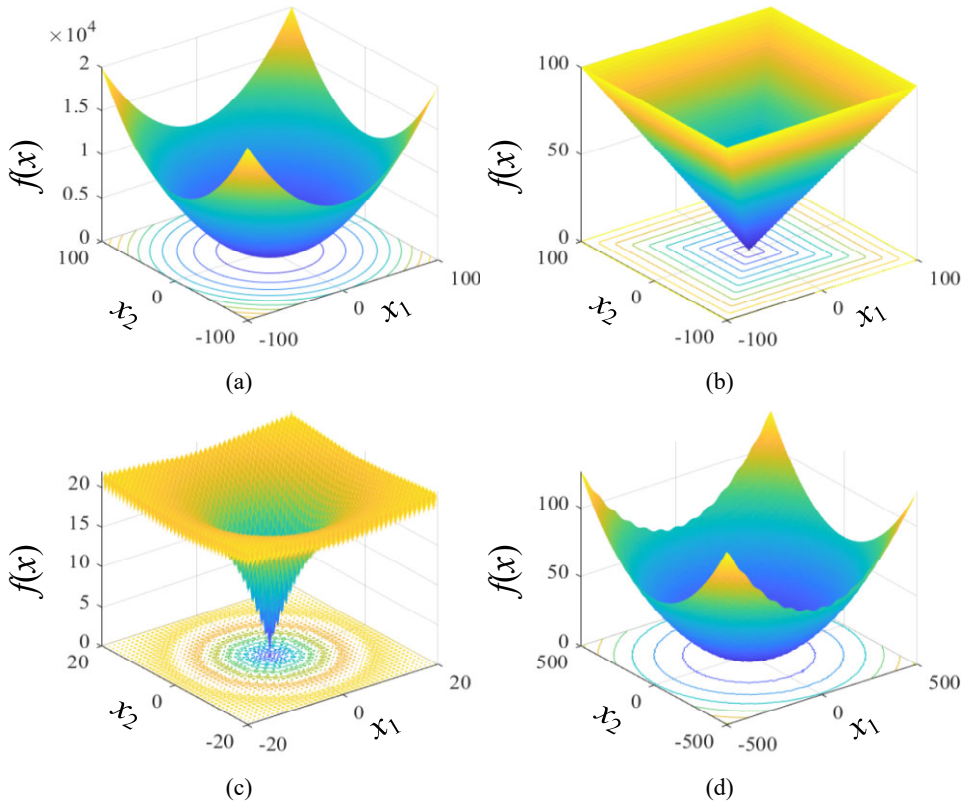


Table 6 Test results of the three algorithms with the four test functions

Function	Algorithm	Number of program runs	Mean	Standard deviation
f_1	PSO	30	5.759×10^{-3}	1.912×10^{-3}
	GWO	30	8.075×10^{-28}	1.024×10^{-27}
	Improved GWO	30	5.185×10^{-42}	8.038×10^{-42}
f_2	PSO	30	1.515×10^{-1}	5.858×10^{-2}
	GWO	30	9.932×10^{-7}	1.440×10^{-6}
	Improved GWO	30	4.557×10^{-11}	7.247×10^{-11}
f_3	PSO	30	1.103	6.896×10^{-1}
	GWO	30	1.107×10^{-13}	1.486×10^{-14}
	Improved GWO	30	8.704×10^{-15}	2.132×10^{-15}
f_4	PSO	30	6.557×10^{-4}	1.963×10^{-4}
	GWO	30	7.422×10^{-3}	1.554×10^{-2}
	Improved GWO	30	0	0

It is seen that the improved GWO algorithm can converge closely to the optimal solution for the Sphere, Schwefel, Ackley, and Griewank functions, and wherein for the Griewank function the accuracy is the highest. For the four test functions, the improved GWO algorithm has the smallest mean value and standard deviation compared with the other two algorithms, and thereby the accuracy and robustness of the algorithm are verified.

Figure 11 to Figure 14 show the evolutionary convergence curves of the three algorithms for the four test functions. It is obvious that for most of the test functions, both the GWO algorithm and the improved GWO algorithm are much more advantageous than the classical PSO algorithm which is easy to fall into the local optimum. Furthermore, the convergence speed of the improved GWO algorithm is slightly faster than that of the GWO algorithm in general, and the accuracy of the improved GWO algorithm is also slightly higher than the GWO algorithm especially for the Griewank function as shown in Figure 13. Overall, the performance of the improved GWO algorithm is better than the classical PSO algorithm and the standard GWO algorithm.

Figure 11 Evolution convergence curves of the three algorithms for the sphere function

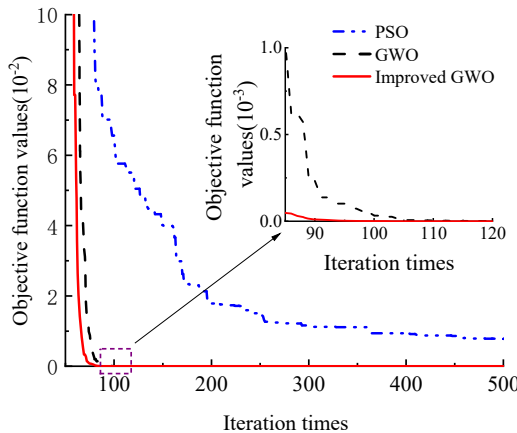


Figure 12 Evolution convergence curve of the three algorithms for the Schwefel function (see online version for colours)

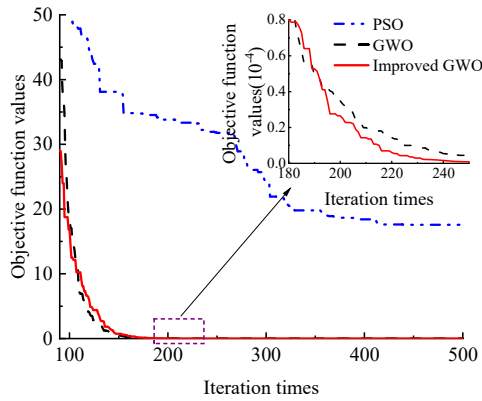


Figure 13 Evolution convergence curve of the three algorithms for the Ackley function (see online version for colours)

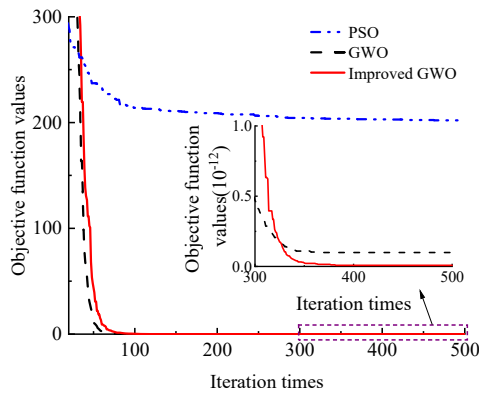
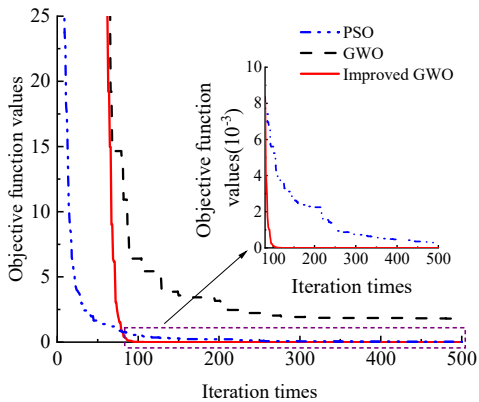


Figure 14 Evolution convergence curve of the three algorithms for the Griewank function (see online version for colours)



5 Optimisation of body frame orienting frontal crashworthiness

5.1 Deterministic optimisation based on the improved GWO algorithm

Based on the dimensions of the driving area recommended in ‘interior dimensions of passenger cars’ (National Standard of China GB/T13053-2008), the intrusion of the three design variables is constrained. By maximising the energy absorption and thus enhancing the frontal crashworthiness performance, the driver’s living space is expected to be increased and the raise of the mass of the optimised area can be limited. The deterministic optimisation mathematical model is expressed as:

$$\begin{aligned}
 &\text{Find } \mathbf{x} = (x_1, x_2, x_3, x_4, x_5)^T \\
 &\text{Min } -E(\mathbf{x}) \\
 &\text{s.t. } \begin{cases} I_1(\mathbf{x}) \leq 450, I_2(\mathbf{x}) \leq 390, \\ I_3(\mathbf{x}) \leq 290, M(\mathbf{x}) \leq 89, \\ x_L \leq x_i \leq x_U, i = 1, 2, \dots, 5 \end{cases}
 \end{aligned} \tag{21}$$

where x_L and x_U represent the lower and upper bound of the design variables with the value of 1 and 10, respectively. The optimisation results for the deterministic optimisation based on the GWO algorithm and the improved GWO algorithm are presented in Figure 15. It can be seen that the improved GWO algorithm is superior to the classic GWO algorithm in both convergence speed and global optimisation. The comparison of the performance before and after optimisation by the two algorithms is shown in Table 7. It is revealed that the total internal energy absorption energy E and the intrusion amount I_1 are greatly improved, and the performance of the other three optimisation responses can also be improved to some extent. In addition, by comparing the performance of optimisation between the two algorithms, in general, more enhancement in performance can be found by the improved GWO algorithm than the GWO before improvement especially for the metrics E and I_1 , though some declines in performances of the two metrics I_3 and M appear.

Figure 15 Optimisation results of the classic GWO and the improved GWO algorithms (see online version for colours)

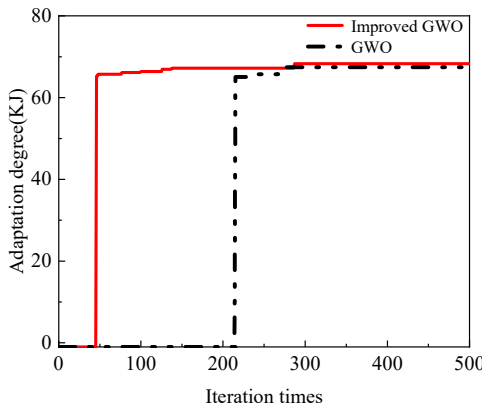


Table 7 Performance comparison before and after optimisation by GWO and the improved GWO algorithms

Optimisation response	Initial value	Optimised value by GWO	Enhancement by GWO	Optimised value by the improved GWO	Enhancement by the improved GWO
$E(J)$	63,128	63,167	0.06%	67,041	6.20%
$I_1(\text{mm})$	452.79	443.48	2.06%	428.89	5.28%
$I_2(\text{mm})$	392.38	388.98	0.87%	388.29	1.04%
$I_3(\text{mm})$	297.11	283.20	4.68%	289.53	2.55%
$M(\text{kg})$	89.35	88.28	1.20%	88.52	0.93%

5.2 Reliability optimisation based on MCS

Considering the complexity and uncertainty in actual situations, such as driving operation, road environment, loading condition, impact load in collision, etc., the reliability optimisation is to be executed after deterministic optimisation based on the MCS method (Chen et al., 2020). Figure 16 and Figure 17 respectively illustrates the principle of reliability optimisation and Monte Carlo sampling.

MCS as a stochastic simulation method based on probability and statistical theory is advantageous in simplicity of calculation and accuracy of results, but it requires a large number of repeated sampling calculations, resulting the low computing efficiency. Considering the influence of the uncertain factors in practical situations, the five design variables obtained by the deterministic optimisation are further assumed to follow the normal distribution, and the coefficient of variation is 1% (Gu et al., 2013). For each design variable, 10,000 sample points are collected and are brought into the response surface surrogate model to calculate the corresponding optimal response. Then, the reliability of each response (as shown in Table 8) is obtained based on the proportion of optimal responses that satisfy the constraints in the total number.

Figure 16 Principle of reliability optimisation

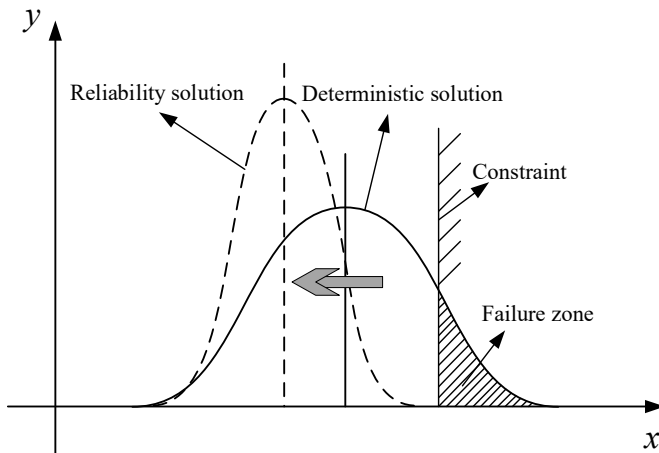


Figure 17 Principle of Monte Carlo sampling (see online version for colours)

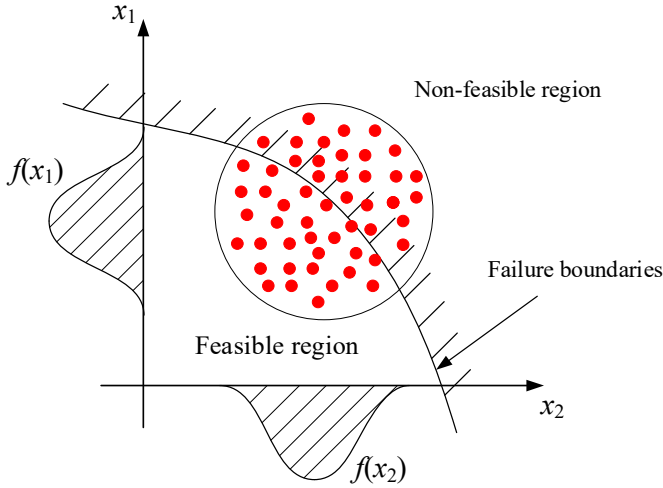


Table 8 Reliability analysis for the deterministic optimisation

Response and constraints	Deterministic optimisation	
	Optimal solution	Reliability
$I_1 \leq 450$ mm	428.89	100%
$I_2 \leq 390$ mm	388.29	89.30%
$I_3 \leq 290$ mm	289.53	63.55%
$M \leq 89$ kg	88.52	100%

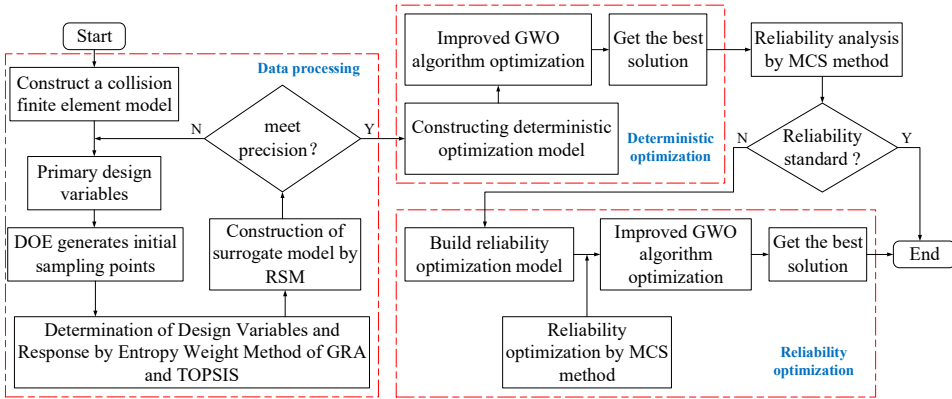
It can be seen from Table 7 that the reliability of the optimised responses I_2 and I_3 are only 89.30% and 63.55%. The reliability is less than 90%, which means that the optimal solution of the deterministic optimisation design is extremely unstable. When the uncertainty is considered, the optimisation response would be easy to exceed the constraints. Therefore, it is necessary to execute reliability optimisation on the basis of deterministic optimisation. The mathematical model of reliability optimisation is formulated as follows:

$$\begin{aligned}
 &\text{Find } \mathbf{x} = (x_1, x_2, x_3, x_4, x_5)^T \\
 &\text{Min } -E(\mathbf{x}) \\
 &\text{s.t. } \begin{cases} P[I_1(\mathbf{x}) \leq 450] \geq R \\ P[I_2(\mathbf{x}) \leq 390] \geq R \\ P[I_3(\mathbf{x}) \leq 290] \geq R \\ P[M(\mathbf{x}) \leq 89] \geq R \\ x_L \leq x_i \leq x_U, \quad i = 1, 2, 3, 4, 5 \end{cases} \quad (22)
 \end{aligned}$$

where R is valued at 90%, 95% and 99% respectively to evaluate the influence of different reliability on the optimisation results, that is, the probability that the constraints violate the boundary under uncertain factors is 10%, 5% and 1%, respectively.

Here, the reliability optimisation is also performed by the method of MCS. The solutions that meet the reliability conditions are sampled and then the final solutions that meet the specified value of reliability can be obtained. Ultimately, the improved GWO algorithm is employed to search the optimal solution. The flow chart of the overall reliability optimisation is illustrated by Figure 18.

Figure 18 Reliability optimisation flow chart (see online version for colours)



The target response values obtained by the three reliability optimisations are 65275J, 66053J and 64187J, which are slightly smaller than the deterministic optimal solution. It means that for the reliability optimisation, with the increasing of the reliability value, the optimisation performance of some target extreme values would be sacrificed to obtain a compromise solution that satisfies the reliability. Seen from the reliability optimisation results listed in Table 9, it is observed that with the increasing of reliability, each response gradually moves away from the constraint boundary, and the obtained results are in line with the expectations. To achieve the highest total internal energy absorption of the objective function value, 95% reliability is chosen as the final optimisation scheme in this study.

Table 10 illustrates the optimised results of the five design variables, including the results of deterministic optimisation and 95% reliability optimisation. It can be observed that design variable x_1 changes little before and after optimisation, and both the variable x_2 and x_4 have decreased after optimisation, while x_3 and x_5 both have increased. Therefore, it can be concluded that the changes between the design variables in the optimisation present a compromise characteristics, which is consistent with the expectations.

In Table 10, the optimised values of the design variables are rounded for the actual manufacturing requirement. The influence of the rounded values on the reliability of optimisation is evaluated and shown in Table 11. It can be seen that for the deterministic optimisation, the reliability of the optimisation responses I_2 and I_3 declines after the optimised values being rounded comparing with the corresponding reliability result in Table 8. While for the reliability optimisation, the reliability for I_3 and I_4 declines and rises respectively comparing with the corresponding result of the case of 95% reliability optimisation in Table 9. That is, the rounded values do have some effect on the reliability, but it is still acceptable since the difference is relatively small.

Table 9 Reliability optimisation results

Response and constraints	90% reliability optimisation		95% reliability optimisation		99% reliability optimisation	
	Mathematical expectation	Reliability	Mathematical expectation	Reliability	Mathematical expectation	Reliability
$I_1 \leq 450$ mm	442.93	100%	434.06	100%	439.75	100%
$I_2 \leq 390$ mm	388.75	94.77%	381.04	100%	388.35	99.99%
$I_3 \leq 90$ mm	288.48	100%	286.83	99.42%	284.90	100%
$M \leq 89$ kg	88.65	100%	88.77	97.75%	88.60	99.72%

Table 10 Comparison of design variables before and after optimisation

Design variable	Initialising value(mm)	Deterministic optimisation(mm)		Reliability optimisation(mm)	
		Optimisation value	Rounded value	Optimisation value	Rounded value
x_1	1.5	1.506	1.5	1.413	1.4
x_2	1.5	1.0	1.0	1.0	1.0
x_3	1.5	2.054	2.1	2.096	2.1
x_4	2.0	1.746	1.7	1.736	1.7
x_5	1.0	1.680	1.7	1.576	1.6

Table 11 Reliability of optimisation by the rounded variable values

Performance constraints	Deterministic optimisation (mm)		Reliability optimisation (mm)	
	Mathematical expectation	Reliability	Mathematical expectation	Reliability
$I_1 \leq 450$ mm	427.71	100%	432.66	100%
$I_2 \leq 390$ mm	388.58	83.4%	382.75	100%
$I_3 \leq 290$ mm	292.52	23.0%	288.06	94.53%
$M \leq 89$ kg	88.32	100%	88.54	100%

6 Crashworthiness analysis before and after optimisation

To further evaluate the optimisation effect, a group of finite element analysis is conducted with the reliability optimisation results, and the displacement contour plots of frontal collision before and after optimisation are obtained, which are shown in Figure 19. It is observed that though the reliability optimisation results are relatively conservative, the collision safety is significantly improved. Figure 20 shows the intrusion at the three measurement points during the collision.

Note that during the collision the intrusions at the three measuring points all rise first and tend to be roughly stable finally. The measurement point I_2 located at the front of the cockpit, and the measuring point I_3 located at the rear of the cockpit are both subjected to a relatively long-duration deformation, where the intrusions have kept increasing for about 50ms. It is mainly attributed to the large potential and space of deformation of the

components and structures around the two measuring points. While for the measuring point I_1 located in the centre of the steering wheel, the duration time of deformation is relatively short and the time of increasing of intrusion is about 40ms. Furthermore, the maximum intrusion I_1 , I_2 and I_3 is reduced from 452.8mm to 434.1mm, from 392.4mm to 381.0mm, and from 318.4mm to 286.8mm, respectively. That is intrusions at the three measurement points after optimisation are significantly reduced, and thus the driver's living space is expected to be considerably improved.

In addition, it can also be found in Figure 20 that the intrusion I_1 for the reliability optimisation is slightly larger than that of the deterministic optimisation, but is smaller than that of the original design. For the intrusions I_2 and I_3 , the amount of the reliability optimisation is smaller than that of the deterministic optimisation. From the comparison of the total internal energy absorption of the optimising design region shown in Figure 21, it can be found that both deterministic optimisation and reliability optimisation can make the obtained target value more optimal. Additionally, higher reliability requirements will reduce the extreme value of the objective function. After the reliability optimisation, the total internal energy absorption increases from 63128J to 66053J with an increment of 4.63%, and the performance of crashworthiness safety is considerably enhanced.

Figure 19 Displacement contour plots of frontal collision before and after optimisation, (a) original design (b) deterministic optimisation (c) reliability optimisation (see online version for colours)

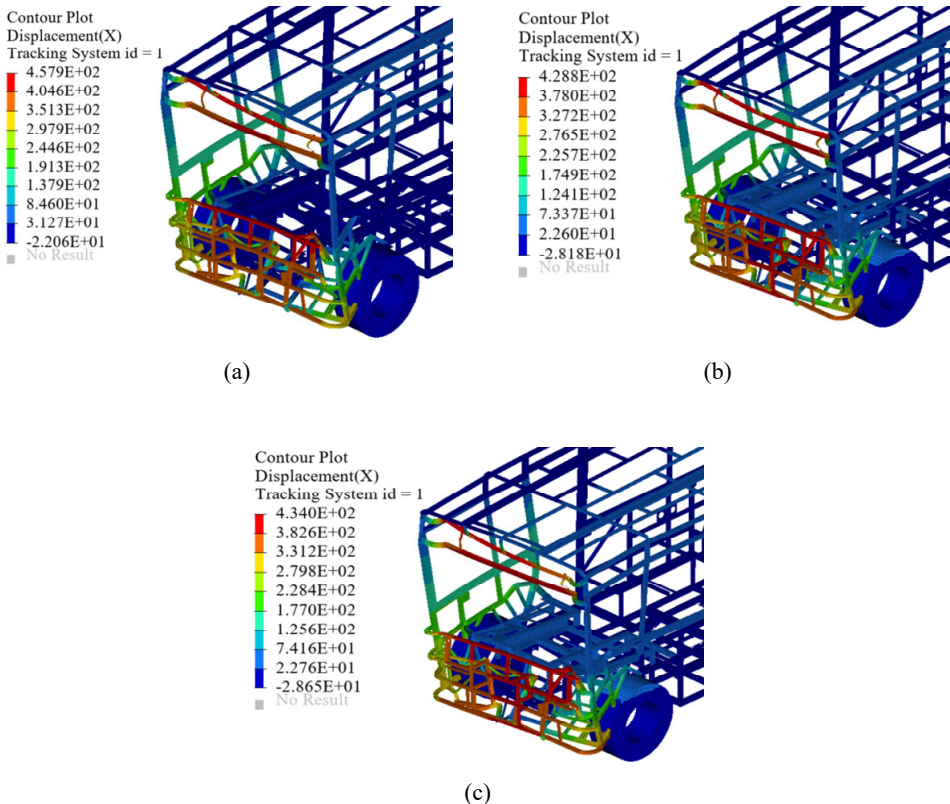


Figure 20 Comparison of the intrusions at the three measurement point (see online version for colours)

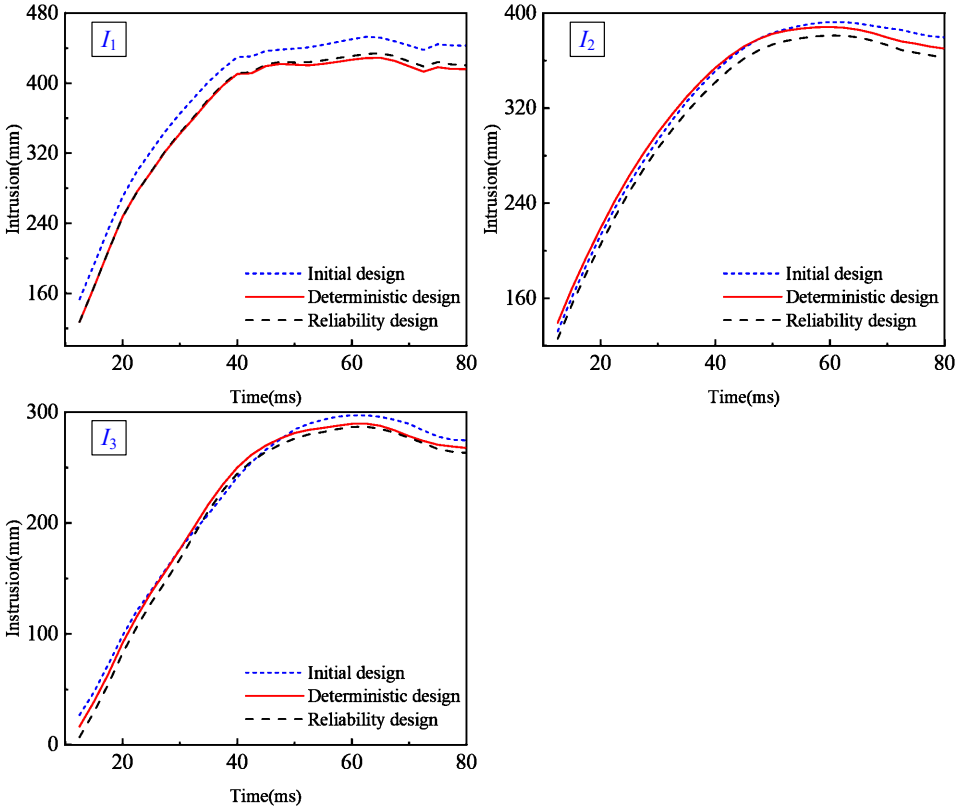
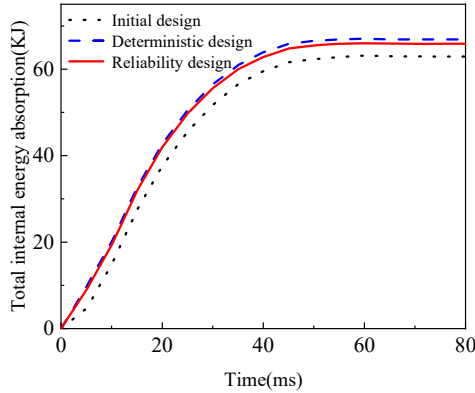


Figure 21 Comparison of the total internal energy absorption in the area of optimisation (see online version for colours)



7 Conclusions

Crashworthiness has always been an important part of the research on the safety of the commercial bus. To improve the performance of frontal crashworthiness, a reliability design method based on the improved grey wolf algorithm combined with MCS is proposed in this paper. By leveraging the Tent chaotic map to generate the initial population and utilising the Sigmoid function to improve the convergence factor, the grey wolf algorithm is improved and applied to the design optimisation of the body frame of an electric bus in this paper. After obtaining the deterministic optimal solution, the reliability of the response results is evaluated by combining it with the MCS method. Then, under the corresponding reliability requirements, the mathematical expectation of each response is derived, and then the reliability optimisation variables are obtained by the improved GWO algorithm.

The results reveal that, on the one hand, the improvement in convergence speed and searching of optimal solution by the improved GWO is obvious compared with the GWO algorithm. On the other hand, although the reliability-optimised design scheme tends to be conservative, compared with the initial scheme, the performance of frontal crashworthiness of the bus body frame is still improved, and thereby the feasibility of the optimised design scheme in this paper is verified. Unfortunately, the reliability results given by the surrogate model in this work have not been verified by the FE model, and thus we are uncertain how accurate the reliability results would be at the current stage. This will be done in our subsequent research work.

Acknowledgements

This project was supported by the National Natural Science Foundation of China (NSFC) (51465023). The authors much appreciate the financial support.

References

- Al-Omari, R., Somani, A.K. and Manimaran, G. (2005) 'An adaptive scheme for fault-tolerant scheduling of soft real-time tasks in multiprocessor systems', *Journal of Parallel and Distributed Computing*, Vol. 65, No. 5, pp.595–608.
- Chen, Y., Liu, X., Shan, Y. and He, T. (2020) 'Lightweight design of drive axle housing based on reliability', *International Journal of Vehicle Performance*, Vol. 6, No. 3, pp.294–309.
- Chen, Z., Qiu, H., Gao, L. and Li, P. (2013) 'An optimal shifting vector approach for efficient probabilistic design', *Structural and Multidisciplinary Optimization*, Vol. 47, No. 6, pp.905–920.
- Deb, K., Agrawal, S., Pratap, A. and Meyarivan, T. (2000) 'A fast elitist non-dominated sorting genetic algorithm for multi-objective optimization: NSGA-II', *International Conference on Parallel Problem Solving from Nature*, Springer, Berlin, Heidelberg, September, pp.849–858.
- Gaidhane, P.J. and Nigam, M.J. (2018) 'A hybrid grey wolf optimizer and artificial bee colony algorithm for enhancing the performance of complex systems', *Journal of Computational Science*, Vol. 27, pp.284–302.
- Gu, X., Dai, J., Huang, X. and Li, G. (2017) 'Reliable optimisation design of vehicle structure crashworthiness under multiple impact cases', *International Journal of Crashworthiness*, Vol. 22, No. 1, pp.26–37.

- Gu, X., Sun, G., Li, G., Mao, L. and Li, Q. (2013) 'A comparative study on multiobjective reliable and robust optimization for crashworthiness design of vehicle structure', *Structural and Multidisciplinary Optimization*, Vol. 48, No. 3, pp.669–684.
- Gurumoorthy, S., Arunachalam, M., Oery, T. and Mohan, S. (2020) *Automotive Wheel Metamodeling Using Response Surface Methodology (RSM) Technique*, No. 2020-01-1234, SAE Technical Paper, SAE International, Warrendale, Pennsylvania, USA.
- Huang, Z.L., Jiang, C., Zhou, Y.S., Zheng, J. and Long, X.Y. (2017) 'Reliability-based design optimization for problems with interval distribution parameters', *Structural and Multidisciplinary Optimization*, Vol. 55, No. 2, pp.513–528.
- Kamboj, V.K. (2016) 'A hybrid grey wolf optimizer and artificial bee colony algorithm for enhancing the performance of complex systems', *Neural Computing and Applications*, Vol. 27, No. 6, pp.1643–1655.
- Kennedy, J. and Eberhart, R. (1995) 'Particle swarm optimization', *Proceedings of ICNN'95-International Conference on Neural Networks*, November, IEEE, Vol. 4, pp.1942–1948.
- Li, X., Wang, Z., Zhang, L., Zou, C. and Dorrell, D.D. (2019) 'State-of-health estimation for Li-ion batteries by combing the incremental capacity analysis method with grey relational analysis', *Journal of Power Sources*, Vol. 410, pp.106–114.
- Long, W., Jiao, J., Liang, X. and Tang, M. (2018) 'An exploration-enhanced grey wolf optimizer to solve high-dimensional numerical optimization', *Engineering Applications of Artificial Intelligence*, Vol. 68, pp.63–80.
- Long, W., Jiao, J., Liang, X., Cai, S. and Xu, M. (2019) 'A random opposition-based learning grey wolf optimizer', *IEEE Access*, Vol. 7, pp.113810–113825.
- Lv, X., Huang, X., Gu, X., Liu, W. and Li, G. (2016) 'Reliability-based multiobjective optimisation of vehicle bumper structure holes for the pedestrian flexible legform impact', *International Journal of Crashworthiness*, Vol. 21, No. 3, pp.198–210.
- Mirjalili, S., Mirjalili, S.M. and Lewis, A. (2014) 'Grey wolf optimizer', *Advances in Engineering Software*, Vol. 69, pp.46–61.
- Mittal, N., Singh, U. and Sohi, B.S. (2016) 'Modified grey wolf optimizer for global engineering optimization', *Applied Computational Intelligence and Soft Computing*, Vol. 2016, Article ID 7950348, pp.1–16.
- Qin, X. and Jiang, H. (2006) 'A novel fault-tolerant scheduling algorithm for precedence constrained tasks in real-time heterogeneous systems', *Parallel Computing*, Vol. 32, Nos. 5–6, pp.331–356.
- Salmani, H., Khalkhali, A. and Ahmadi, A. (2022) 'Multi-objective optimization of vehicle floor panel with a laminated structure based on V-shape development model and Taguchi-based grey relational analysis', *Structural and Multidisciplinary Optimization*, Vol. 65, No. 3, pp.1–23.
- Shan, L., Qiang, H., Li, J. and Wang, Z. (2005) 'Chaotic optimization algorithm based on tent map', *Control and Decision*, Vol. 20, No. 2, p.179, DOI: 103321/jissn: 1001-0920.2005.02.013.
- Sun, G., Li, G., Zhou, S., Li, H., Hou, S. and Li, Q. (2011) 'Crashworthiness design of vehicle by using multiobjective robust optimization', *Structural and Multidisciplinary Optimization*, Vol. 44, No. 1, pp.99–110.
- Teng, Z., Lv, J., Guo, L. and Xu, Y. (2018) 'An improved hybrid grey wolf optimization algorithm based on tent mapping', *Journal of Harbin Institute of Technology*, Vol. 50, No. 11, pp.40–49.
- Wei, Z., Zhao, H., Han, B., Sun, C. and Li, M. (2017) 'Grey wolf optimization algorithm with self-adaptive searching strategy'. *Computer Science*, Vol. 44, No. 3, pp.259–263.
- Xia, L., Liu, W., Lv, X. and Gu, X. (2018) 'A system methodology for optimization design of the structural crashworthiness of a vehicle subjected to a high-speed frontal crash', *Engineering Optimization*, Vol. 50, No. 4, pp.634–650.

- Xu, C., Li, C., Yu, X. and Huang, Q. (2017) 'Improved grey wolf optimization algorithm based on chaotic cat mapping and Gaussian mutation', *Computer Engineering and Applications*, Vol. 53, No. 4, pp.1–9.
- Zhang, X. and Wang, X. (2019) 'Comprehensive review of grey wolf optimization algorithm', *Computer Science*, Vol. 46, No. 3, pp.30–38.
- Zhu, A., Xu, C., Li, Z., Wu, J. and Liu, Z. (2015) 'Hybridizing grey wolf optimization with differential evolution for global optimization and test scheduling for 3D stacked SoC', *Journal of Systems Engineering and Electronics*, Vol. 26, No. 2, pp.317–328.